Open Ceramics 20 (2024) 100688

Contents lists available at ScienceDirect

Open Ceramics

journal homepage: www.sciencedirect.com/journal/open-ceramics

Synthesis of polycrystalline Ta_2O_5 inverse opal photonic crystal powders and their optical characterization

Taiki Maekawa [a], Hiroyuki Maekawa [b], Yuto Ikeda [a], Tomoya Onoe [a], Geoffrey I.N. Waterhouse [c], Kei-ichiro Murai [a], Toshihiro Moriga [a,*]

[a] Department of Applied Chemistry Course, Graduate School of Science and Technology for Innovation, Tokushima University, 2-1 Minami-Josanjima, Tokushima, 770-8506, Japan
[b] Department of Chemistry and Life Science, Yokohama National University, 79-5 Tokiwadai, Hodogaya-ku, Yokohama-shi, Kanagawa, 240-8501, Japan
[c] School of Chemical Science, The University of Auckland, Private Bag, 92019, Auckland, New Zealand

ARTICLE INFO

Handling Editor: Dr P Colombo

Keywords:
Inverse opal
Photonic band gap
Structural color

ABSTRACT

Polycrystalline Ta_2O_5 inverse opal (IO) photonic crystal powders were synthesized using PMMA colloidal crystals as sacrificial templates. We prepared Ta_2O_5 IO powders with vibrant structural colors at UV–vis wavelengths. The photonic bandgaps (PBGs) in the Ta_2O_5 IO powders red-shifted as a function of both the macropore diameter and the refractive index of the medium filling the macropores. Owing to their polycrystalline structure, the Ta_2O_5 IO powders exposed PBGs for various FCC facets, making investigation of their optical properties significantly more complex than Ta_2O_5 IO thin films that preferentially expose only (111) planes as studied previously. Due to the overlap of the PBGs from different FCC facets and the defects that cause light scattering, much of the typical angle-dependent structural color observed in IO thin films was lost in the Ta_2O_5 IO powders. This study offers new insights into the optical properties of IO powders.

1. Introduction

Tantalum-based semiconductors have many advantages, including tunable electronic band gaps, high refractive indices, high dielectric constants, and good stability, thus finding applications as photocatalysts, scintillators, phosphors, gas sensors, and capacitors [1–5]. In most of these applications, semiconductor materials with a large surface area are advantageous. Toward enhancing the surface area of tantalum-based semiconductors, while also looking to improve the light absorption efficiency by harnessing "slow photon" phenomena, researchers are now seeking to use colloidal crystal templating approaches to engineer large-surface-area inverse opal (IO) photonic crystal (PhC) materials (comprising face-centered cubic (FCC) arrays of macropores in a semiconducting dielectric matrix).

The concept of PhCs was first introduced in 1987 by Yablonovich et al. [6–8]. A PhC is a material with a periodically-modulated refractive index that can be prepared in 1D, 2D, or 3D forms. Such a periodic structure enables the formation of photonic bandgaps (PBGs) that inhibit light propagation at specific wavelengths, leading to the diffraction of light over a narrow range of wavelengths [9,10]. The PBG position depends on the periodicity and average refractive index of the PhC, and the angle of incidence. The optical properties of most PhCs can be described using the modified Bragg's law equation that considers both light refraction and diffraction in the PhC. When the periodicity in a PhC is approximately a few hundred nanometers (i.e., around half the wavelength of visible light), PBGs will emerge at visible wavelengths, giving rise to a visible structural color (i.e., color that originates from the diffraction of light, rather than a pigment-based color arising from electronic transitions). At the edges of the PBGs, light propagates with a significantly reduced group velocity, creating "slow photons" that can be harnessed to improve photocatalysis or suppress spontaneous emission in semiconductors [11–13]. Further, the iridescence or angle-dependent colors of PhCs make them desirable as colorants [10,14,15]. Furthermore, the existence of photonic band gaps (PBGs) in opal and inverse opals allows the creation of optical sensors, since the PBG frequencies are sensitive to the refractive index of the surrounding medium.

Colloidal crystal templating is a cost-effective method for fabricating semiconductor PhCs. This method involves the crystallization of submicron-sized monodisperse polymethyl methacrylate (PMMA) or

* Corresponding author.
E-mail address: moriga@tokushima-u.ac.jp (T. Moriga).

https://doi.org/10.1016/j.oceram.2024.100688
Received 18 July 2024; Received in revised form 2 September 2024; Accepted 29 September 2024
Available online 30 September 2024

Table 1
Conditions used for the synthesis of PMMA colloids of different diameters.

Batch	Volume MMA (mL)	Volume Milli-Q (mL)	Mass initiator (g)	Temperature (°C)	D_{PMMA} (nm)
(A)	30	400	0.3750	80	221
(B)	80	400	0.3750	80	297
(C)	100	400	0.3750	80	341
(D)	100	400	0.3750	75	380
(E)	100	350	0.1875	70	401

polystyrene (PS) colloids on a FCC lattice to form a colloidal crystal template that is 74 % solid by volume. The interstitial voids in the template are then filled with a semiconductor precursor solution. After careful drying and calcination in the temperature range of ~500–600 °C to remove the polymer template, a semiconductor IO is obtained with a solid volume fraction <26 % [16,17]. This approach allows for the synthesis of a diverse array of semiconducting IO materials (simply by changing the precursor used during the infiltration step) and offers good control over the surface area, macroporosity, and PBG positions in IO replicas [18,19].

In recent years, there have been many reports on the use of IO architectures to improve photocatalysis or light emission by phosphors, though most of these studies were performed on thin films [20–23]. Most researchers avoided the use of PhC powders because their PBG positions are less well-defined than those in thin films, i.e., the PBG positions depend on the FCC plane and angle of incidence with respect to the surface normal. Waterhouse et al. extensively studied the optical properties of IO metal oxide thin films [24–28], including a recent comprehensive study on the optical properties of Ta_2O_5 IO films and their use in optical sensors [28]. However, optical studies on Ta_2O_5 IO powders are limited [29–31], though there have been some studies on the optical properties of TiO_2, SiO_2, ZrO_2, and NiO IO powders, and their structural colors have been reported [15,32,33]. In many applications involving tantalum-based semiconductors, such as photocatalysis and solar cells, the preferred method to use these semiconductors is in a powdered form owing to the ease of processability and ability to maximize light exposure. This motivated us to perform a detailed study on the optical properties of Ta_2O_5 IO powders.

In this study, Ta_2O_5 IO powders with different macropore diameters were successfully synthesized using the PMMA colloidal crystal templating method. By impregnating PMMA colloidal crystal templates with a tantalum (V) precursor under reduced pressure, we prepared vibrantly colored polycrystalline Ta_2O_5 IO powders. The effects of the macropore diameter (D), angle of incidence, and refractive index of the medium filling the macropores on the PBG positions and structural colors of the various Ta_2O_5 IO powders were systematically investigated. To the best of our knowledge, this is one of the most comprehensive investigations on the optical properties of Ta_2O_5 IO powders reported to date.

2. Experimental

2.1. Materials

Methyl methacrylate (MMA, >98.0 % purity) and 2,2′-azobis (2-methylpropionamidine)dihydrochloride (AAPH) were purchased from FUJIFILM Wako Pure Chemical Co., Ltd. Tantalum pentachloride ($TaCl_5$, 99.9 % purity) was purchased from Kojundo Chemical Co., Ltd. Ethanol (99.5 % purity), methanol (99.8 % purity), 2-propanol (99.7 % purity), toluene (99.5 % purity), and tetraethoxysilane (95 % purity) were purchased from Kanto Chemical Co., Ltd.

2.2. Synthesis of PMMA colloidal suspension and colloidal crystal templates

Suspensions of monodisperse PMMA colloids were synthesized through the surfactant-free emulsion polymerization of the MMA monomer [1,24–28]. The inhibitor in the MMA monomer was first removed via vacuum distillation. Milli-Q water and MMA monomer were added to a four-necked round-bottomed flask fitted with a reflux condenser, a mechanical stirrer, an N_2 inlet valve, and a thermometer. The emulsion was heated to 70, 75, or 80 °C in N_2 atmosphere under vigorous stirring, whereupon the azo initiator was added, and the reaction was allowed to continue for 3 h. The diameters of the PMMA colloids were controlled by varying the amount of MMA monomer and the reaction temperature used in the colloid synthesis (Table 1).

2.3. Synthesis of polycrystalline Ta_2O_5 IO powders

The PMMA colloidal suspensions were centrifuged at 1500 rpm for 24 h, after which the supernatant was discarded. The PMMA colloidal crystals were then carefully dried at 50 °C and used to synthesize Ta_2O_5 IO powders. To prepare the Ta_2O_5 IO powder, 20 wt % $TaCl_5$/ethanol solution was used as the tantalum-containing precursor. The infiltration of the PMMA colloidal crystals with the tantalum-containing precursor was performed under reduced pressure via drop infiltration or immersion impregnation method under reduced pressure.

Drop infiltration method: PMMA colloidal crystal template pieces were transferred to a Buchner funnel. Under vacuum, the Ta precursor solution was added dropwise to the PMMA colloidal crystal templates through a plastic pipette. Excess precursor solution was removed via vacuum filtration.

Immersion impregnation method: The PMMA colloidal crystal template was immersed in the Ta precursor solution in a screw-capped bottle, which was then placed under vacuum for 1 h. Finally, any excess precursor solution was removed via vacuum filtration.

The infiltrated PMMA/$TaCl_5$ (or, more precisely, PMMA/$Ta(OEt)_5$) composite powders obtained using the drop infiltration and immersion impregnation methods were then dried at room temperature for 24 h, resulting in the formation of PMMA/Ta_2O_5 powders. Next, the PMMA/Ta_2O_5 powders were heated from room temperature to 300 °C at 2 °C/min and held at 300 °C for 2 h, and then heated from 300 °C to 550 °C at 2 °C/min and held at 550 °C for 3 h. This process resulted in the complete removal of the PMMA templates and the formation of three-dimensionally macroporous Ta_2O_5 powders. A SiO_2 IO was also prepared for reference purposes using a method described in Ref. [27].

2.4. Characterization

The surface morphologies of the PMMA colloidal crystals and Ta_2O_5 IO powders were examined using a Hitachi S-4700 field-emission scanning electron microscope (FE-SEM). Before the analysis, the samples were sputter-coated with Pt/Pd to prevent specimen charging during imaging. The phase identification of the powdered samples was performed using X-ray diffraction (XRD). A fully automated horizontal multi-purpose X-ray diffractometer (Rigaku Smart Lab) with a CuKα radiation X-ray source (1.5418 Å) was used to collect the XRD data. The tube voltage, tube current, scan step, scanning speed, and 2θ range were set to 45 kV, 100 mA, 0.020°, 24° min^{-1}, and 5–80°, respectively. Diffuse reflectance (DR) measurements were performed using a double-beam spectrophotometer (JASCO V-670) equipped with a light focusing unit. The powder samples were mounted between two quartz glass plates for the measurements. Absolute reflectance measurements were performed to examine the angular dependence of the PBGs in the samples (JASCO ARSN-917). The angle of incidence was varied from 10° to 60°. Images showing the structural colors of the samples were acquired using an iPhone SE3 and a Keyence digital microscope VH-S30 F/B with a VH-5500 attachment. Thermal analyses were performed on a Shimadzu thermogravimetric analyzer (TGA) (TGA-50/50H) at a heating rate of 10 °C/min in air or nitrogen atmosphere.

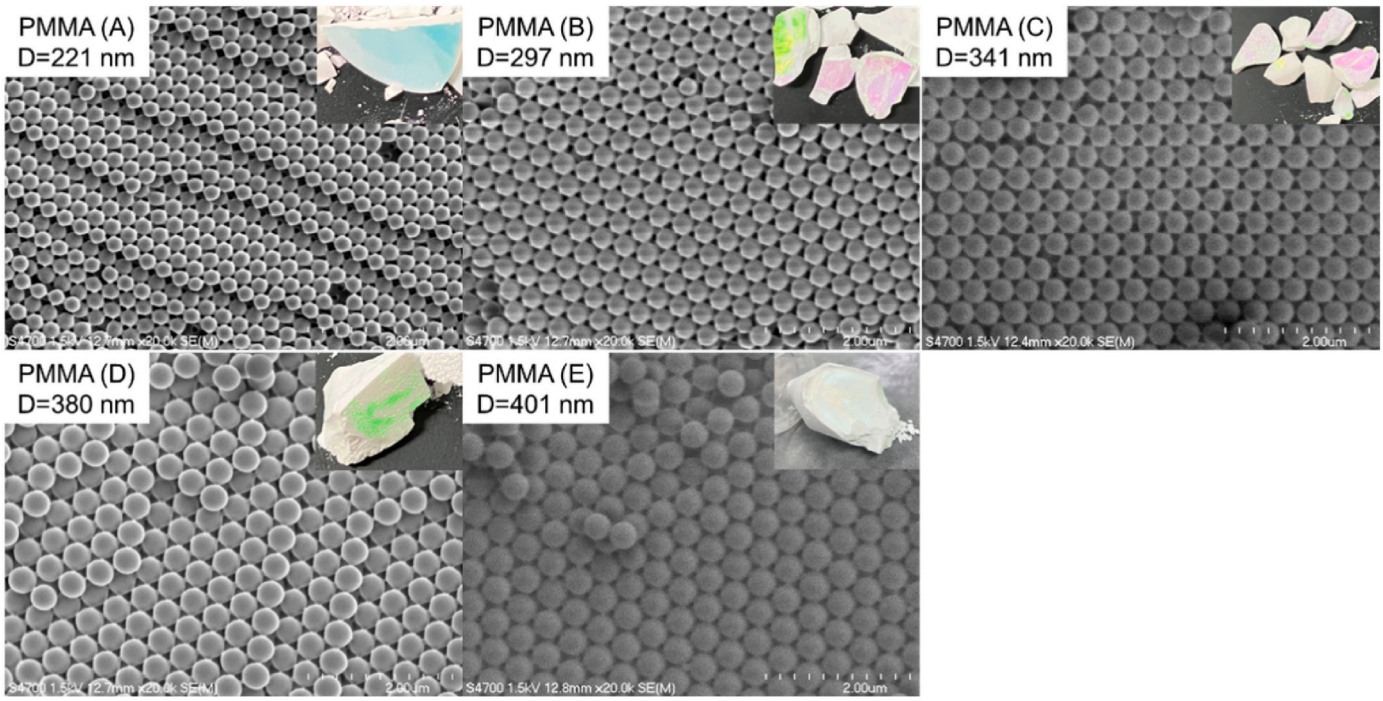

Fig. 1. SEM images of the PMMA colloidal crystal templates prepared from the five batches of PMMA colloids (scale bar 2 μm). The insets show the digital images of the corresponding PMMA colloidal crystals.

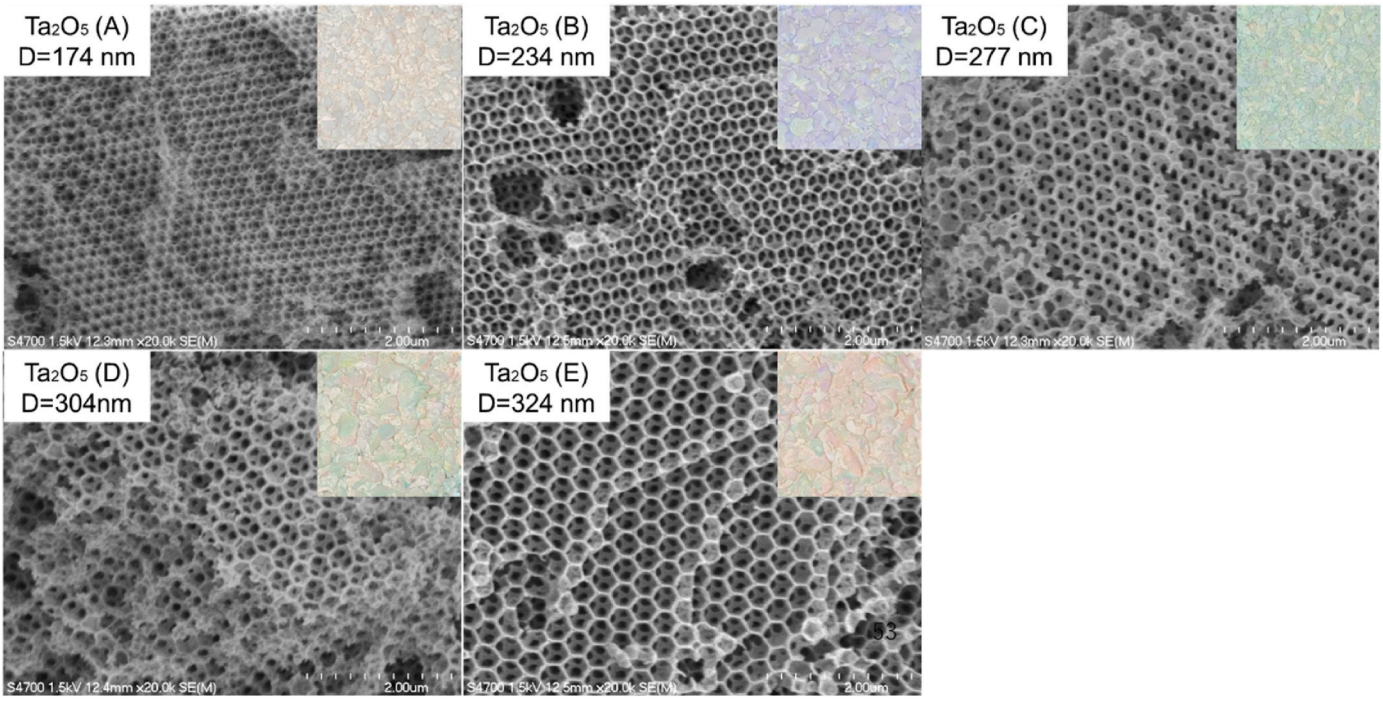

Fig. 2. SEM images of Ta_2O_5 IO powders with different macropore diameters. The insets show digital images of the corresponding Ta_2O_5 IO powders.

3. Results and discussion

Fig. 1 shows the SEM images of the PMMA colloidal crystal templates prepared using five different batches of PMMA colloids. Table 1 lists the synthesis conditions of the PMMA colloids and their diameters estimated from the SEM images using the ImageJ software. The PMMA colloidal diameter (D_{PMMA}) was controlled by changing the reaction temperature and the MMA monomer volume. The PMMA colloid diameter increased with increasing MMA monomer volume and decreasing reaction temperature during the surfactant-free emulsion polymerization. The colloid diameters of the PMMA batches (A), (B), (C), (D), and (E) were 221, 297, 341, 380, and 401 nm, respectively. The all-colloidal crystal templates prepared using the five batches of PMMA colloids exhibited opalescence, suggesting colloidal size uniformity and crystallization in the FCC lattice. Smaller-diameter PMMA batches, such as (A) and (B), showed very strong opalescence, suggesting the emergence of PBGs

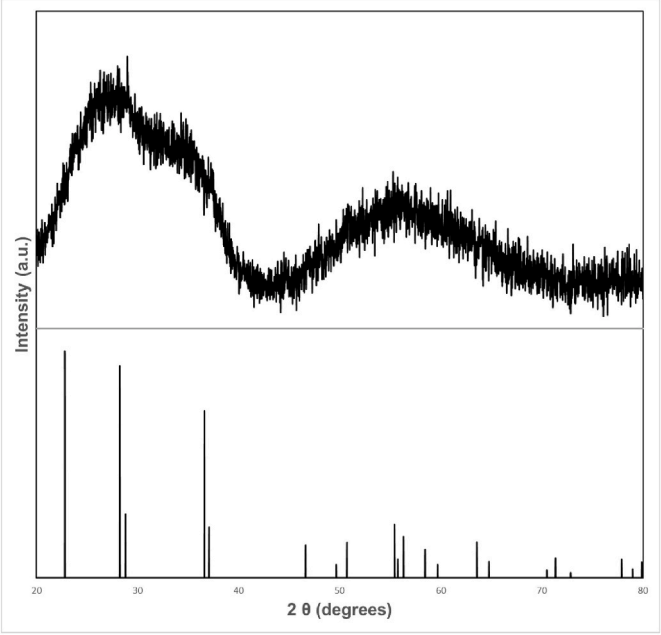

Fig. 3. XRD pattern of the Ta_2O_5 (B) IO powder (upper) and the reference pattern of Ta_2O_5 (PDF card-01-081-8067, lower).

along the [111] direction at visible wavelengths. For the larger batches of colloids, i.e., (C) to (E), the [111] PBGs were outside the visible region (in the near-IR); however, owing to the angle dependence of the PBGs off the PMMA colloidal crystals, some visible color was evident at the grazing angles.

Fig. 2 shows the SEM and digital images of the Ta_2O_5 IO powders prepared using five batches of PMMA colloidal crystals. The Ta_2O_5 IO macropore diameters were measured from the SEM images using the ImageJ software. The macropore diameters of Ta_2O_5 IO (A), (B), (C), (D), and (E) powders were 174, 239, 277, 304, and 324 nm, respectively. These macropore diameters were approximately 80 % of the corresponding colloid diameters in the PMMA colloidal crystal templates, suggesting substantial shrinkage of the FCC lattice during IO formation. However, the Ta_2O_5 IO powders showed ordered arrays of interconnected macropores, confirming a successful templating procedure.

Fig. 3 shows the XRD pattern of Ta_2O_5 IO. The sample was amorphous or possibly nanocrystalline, with very small Ta_2O_5 crystallites. This was expected as the Ta_2O_5/PMMA composite was calcined at a relatively low temperature (550 °C) to remove the PMMA template. The general profile shape of the XRD pattern closely matched the reference pattern for Ta_2O_5 (PDF card-01-081-8067), implying the possible presence of very small Ta_2O_5 crystallites (approximately 1 nm in size) and severe line broadening of the XRD peaks.

Fig. 4 shows the diffuse reflectance spectra, digital microscopic images, and images of Ta_2O_5 (B) IO prepared using the drop infiltration and immersion impregnation methods under reduced pressure. The Ta_2O_5 (B) IO powder synthesized using the drop infiltration method had a white color (characteristic of Ta_2O_5 itself) and almost no structural color. Some light-blue regions can be observed in the digital microscopic image (Fig. 4(b)). Conversely, the Ta_2O_5 (B) IO powder prepared using template impregnation under reduced pressure exhibited a strong blue structural color in both the digital microscopic and optical images (Fig. 4 (c)). The diffuse reflection spectra in Fig. 4(a) show the PBGs of each sample superimposed on a sloping background (black dotted line). A weak PBG peak at 420 nm can be observed in the spectrum of the sample prepared using the drop infiltration method (green line), whereas an intense PBG peak at 440 nm can be observed in the spectrum of the sample prepared using the impregnation method (blue line). Although both the samples were synthesized using the same PMMA template, the PBG positions differed because of the variations in the solid volume fraction of the Ta_2O_5 IOs. The drop infiltration method resulted in poor wetting and infiltration of the template, producing a more disordered structure with a low Ta_2O_5 solid volume fraction. In comparison, impregnation under reduced pressure led to a uniform filling of the PMMA colloidal templates with the Ta (V) precursor because air had already been expelled from the interstitial void spaces. Therefore, the impregnation method resulted in Ta_2O_5 IO powders with larger macropores (because lattice shrinkage was reduced during the calcination step) and higher solid volume fractions. Consequently, the PBG in the Ta_2O_5 (B) IO prepared using the impregnation method under vacuum appeared at longer wavelengths and was more intense than that observed in the Ta_2O_5 (B) IO prepared using the drop infiltration method. In addition, the background (black dotted lines) in the sample prepared using the impregnation method was less pronounced, which enhanced the structural color of the sample. The optical properties of the Ta_2O_5 IOs are discussed in detail below.

Fig. 5 shows the digital images of the Ta_2O_5 (A)–(E) IO powders synthesized using the impregnation method. In air, Ta_2O_5 IO powders mainly appeared (A) white, (B) blue, (C) green, (D) green-yellow, and (E) yellow. Ta_2O_5 (A) IO appeared white, which is typical of tantalum (V) oxide, suggesting that the PBGs in this sample were in the UV region because of the small macropore diameter of the sample. In the Ta_2O_5 (B)–(E) IO samples, the macropore diameters were sufficiently large to yield PBGs in the visible region, with the PBG position red-shifting with increasing macropore size (hence, the color changed from blue for Ta_2O_5 (B) IO to yellow-red for Ta_2O_5 (E) IO). The PBGs red-shifted upon filling the macropores in the IO powders with ethanol (refractive index: 1.36),

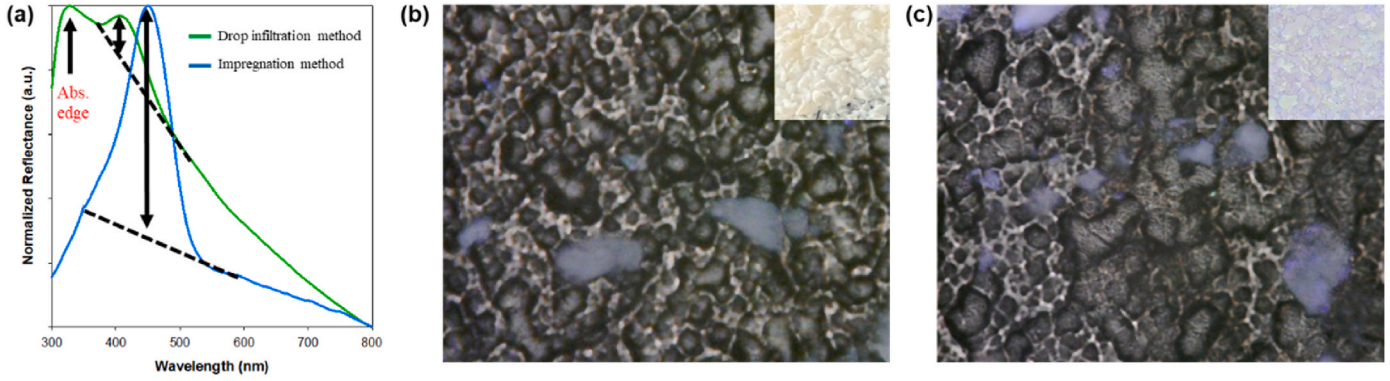

Fig. 4. Optical characterization of Ta_2O_5 (B) IO: (a) UV–Vis spectrum of Ta_2O_5 (B) IO prepared using different synthesis methods, (b) Digital microscopic images of Ta_2O_5 (B) IO synthesized using the drop infiltration method, (c) Digital microscopic image of Ta_2O_5 (B) IO synthesized using the immersion impregnation method. The insets in (b) and (c) show the digital images of each sample.

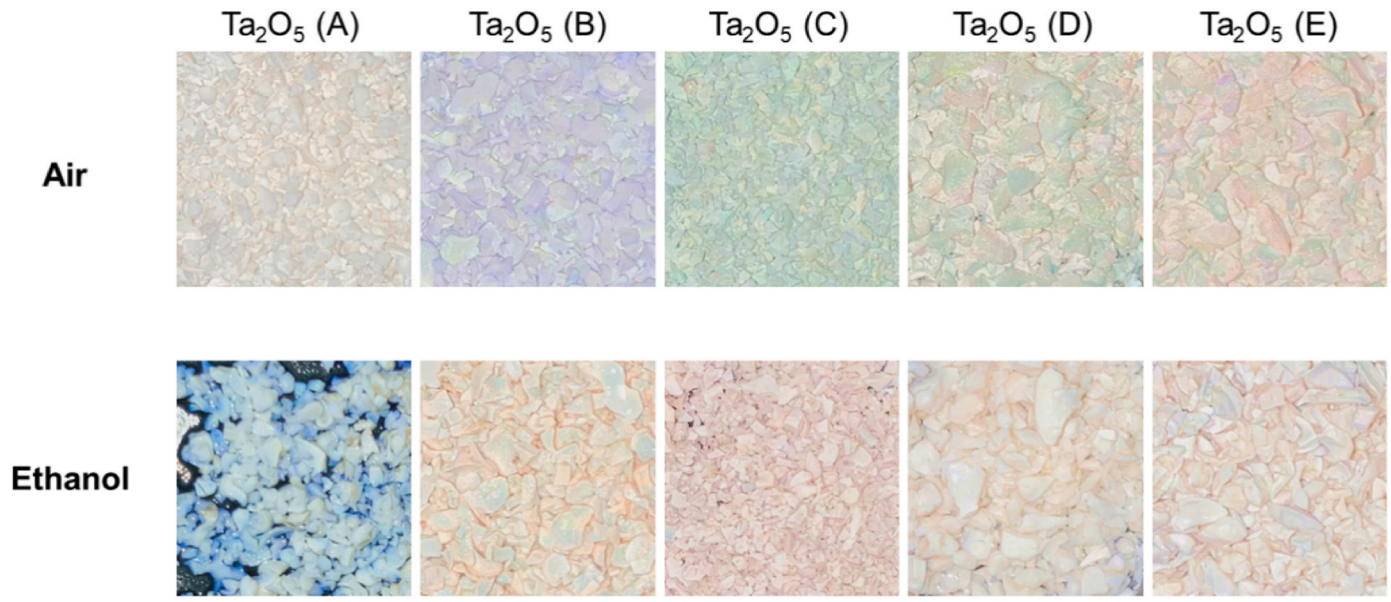

Fig. 5. Digital images of Ta_2O_5 (A)–(E) IO powder samples under white light-irradiation in air (top) and ethanol (bottom).

causing the powders to change their color. When immersed in ethanol, the Ta_2O_5 (A)–(E) IOs appeared blue, green-yellow, red, white, and white, respectively. In this case, the PBGs in the Ta_2O_5 (D) and Ta_2O_5 (E) powders red-shifted to the near-infrared region. The strong structural colors of the samples immersed in air and ethanol confirmed the successful synthesis of good-quality Ta_2O_5 IO PhC powders [34].

Fig. 6(a)–(e) show the diffuse reflection spectra of the Ta_2O_5 IO powders synthesized using the immersion impregnation method under reduced pressure. The insets in Fig. 6 show the optical images of the Ta_2O_5 IO powders. The reflectance spectra were collected in air (green line) and ethanol (blue line) for each sample. It is important to introduce the modified Bragg equation, which is commonly used to describe the optical properties of IOPhCs (see Equation (3)).

$$\lambda_{max} = \frac{2d_{hkl}}{m}\sqrt{(n_{avg})^2 - (sin\,\theta)^2} \quad (1)$$

where λ_{max} is the PBG position (in nm), d_{hkl} is the interplanar spacing (in nm) between the planes with Miller indices *hkl*, m is the order of diffraction, n_{avg} is the average refractive index of the IO, and θ is the incidence angle (in degrees) with respect to the surface normal of the *hkl* planes. For a particular set of FCC planes, the relationship between the interlayer spacing d_{hkl} and macropore diameter (D) in the IOs can be written as follows:

$$d_{hkl} = \frac{\sqrt{2}D}{\sqrt{(h^2 + k^2 + l^2)}} \quad (2)$$

where D is the macropore diameter (nm) of the IO. Considering a first-order diffraction ($m = 1$) and combining Equations (1) and (2), we obtain Equation (3):

$$\lambda_{max} = \frac{2\sqrt{2}D}{\sqrt{(h^2 + k^2 + l^2)}}\sqrt{(n_{avg})^2 - (sin\,\theta)^2} \quad (3)$$

n_{avg} for an IOPhC can be expressed as follows:

$$n_{avg} = \phi_{solid}n_{solid} + (1 - \phi_{solid})n_{void} \quad (4)$$

where ϕ_{solid} is the solid volume fraction of the IO, n_{solid} is the refractive index of the solid material (refractive index of Ta_2O_5 is 2.1), and n_{void} is the refractive index of the material in the macropores (e.g., refractive indices of air and ethanol are 1.000 and 1.361, respectively).

The diffuse reflectance spectra of the Ta_2O_5 IO powders collected in air and ethanol revealed peaks that could be readily assigned to diffraction on the (111), (220), and (311) planes (Fig. 6). Table 2 summarizes the positions of these peaks for the different Ta_2O_5 IO powders. For all the samples, the (111) peak was observed at the longest wavelength, whereas the (220) and (311) peaks were observed at progressively shorter wavelengths, as predicted by Equations (1) and (3). According to Equation (3), the PBG ratio $\lambda_{(220)}/\lambda_{(111)}$ should be $(3)^{1/2}/(8)^{1/2} = 0.612$, while the PBG ratio $\lambda_{(311)}/\lambda_{(111)}$ should be $(3)^{1/2}/(11)^{1/2} = 0.522$, which perfectly matches the observed experimental ratios for each Ta_2O_5 IO powder immersed in both air and ethanol (Table 3). For many of the Ta_2O_5 IO powders in air, the (220) and (311) peaks were below 300 nm and thus outside the range of the spectrometer used in this study (hence not observed). It should also be noted that Ta_2O_5 has an electronic band gap of 3.8–4.0 eV. Therefore, it has a strong absorption below approximately 325 nm, making it difficult to observe the PBGs at such low wavelengths.

The (111) PBGs of the Ta_2O_5 (A)–(E) IO powders in air ($n = 1.00$) were observed at 328, 451, 510, 565, and 595 nm, demonstrating a progressive redshift with increasing macropore diameter in the IOs. Upon immersion in ethanol ($n = 1.36$), the average refractive index of the Ta_2O_5 IO powder increased, with the corresponding (111) PBGs now being observed at 455, 610, 675, 750, and 775 nm. Further, for many of the samples, the (220) and (311) peaks red-shifted to the 300–800 nm region after immersion in ethanol because of the corresponding increase in the n_{avg} value of the PhC. Fig. 6(f) shows that the (111) PBGs in air and both the (111) and (220) PBGs in ethanol red-shifted linearly with the macropore diameter in the Ta_2O_5 IO powders. The modified Bragg's equation (Equation (3)) predicts that the PBG position for a particular FCC plane should increase linearly with the macropore diameter (D) in the inverse opals and also the average refractive index (n_{avg}, which will increase on filling the inverse opals with ethanol) when $\theta = 0°$.

The optical data strongly support the hypothesis that the PMMA colloidal crystals and Ta_2O_5 IO replicas have an FCC structure with an ABC packing arrangement rather than a hexagonal close-packed (HCP) structure with an ABA packing arrangement [35–37].

Fig. 7(a) and (b) show the UV–Vis diffuse reflectance spectra of the Ta_2O_5 (B) IO and Ta_2O_5 (C) IO powders in air ($n = 1.00$) and in different organic solvents, including methanol ($n = 1.329$), ethanol ($n = 1.361$), 2-propanol ($n = 1.377$), and toluene ($n = 1.496$). As expected, the PBGs progressively red-shifted with the increase in the refractive index of the

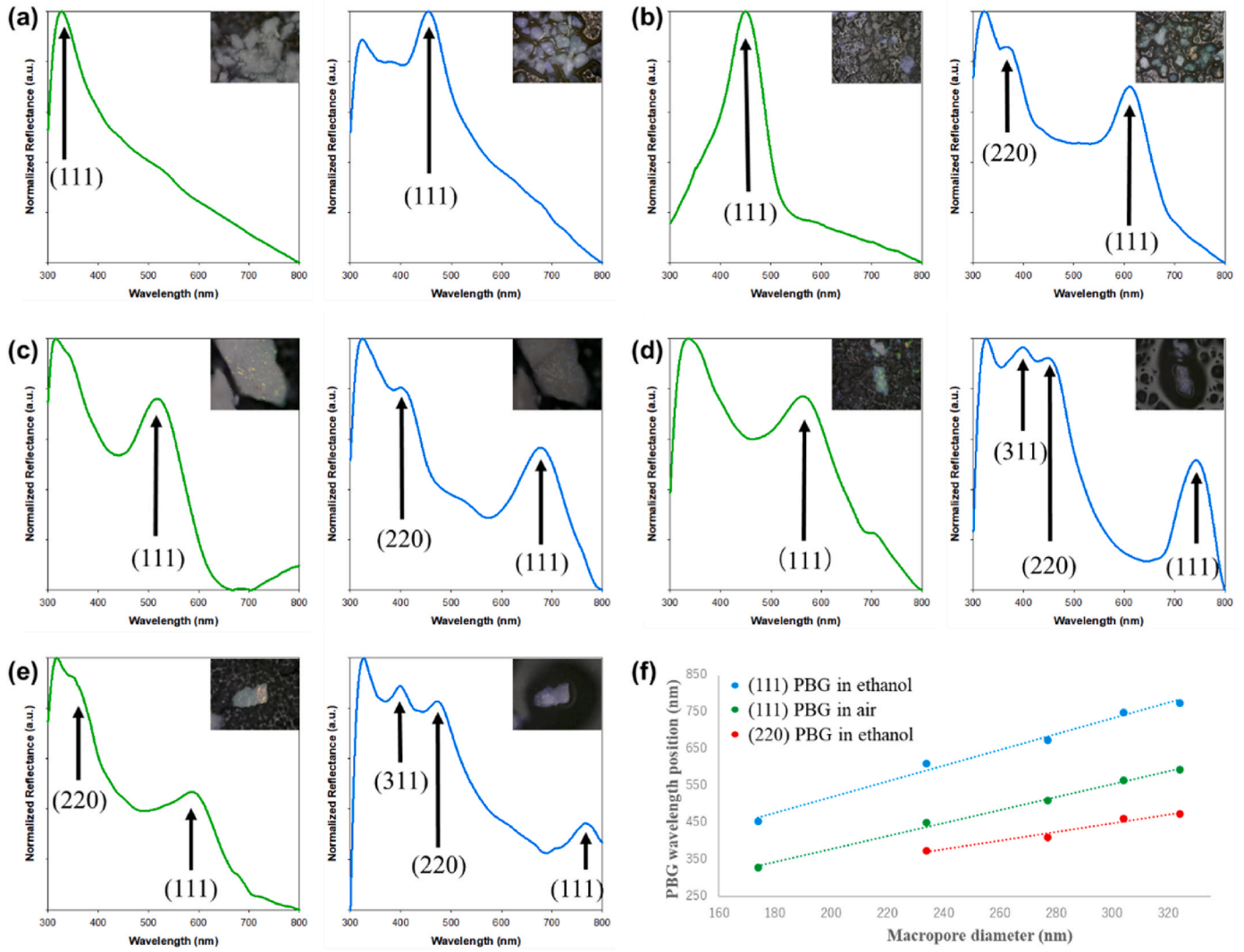

Fig. 6. (a–e): UV–Vis diffuse reflectance spectra of Ta_2O_5 IO powders in air (green line) and ethanol (blue line), (f) linear relationship between the PBG position and macropore diameters for the (111) and (220) PBGs in air and ethanol. (a) Ta_2O_5 (A) IO, (b) Ta_2O_5 (B) IO, (c) Ta_2O_5 (C) IO, (d) Ta_2O_5 (D) IO, and (e) Ta_2O_5 (E) IO.

Table 2
PBG position of Ta_2O_5 (A)–(E) IO samples immersed in air and ethanol.

Sample	D_{Ta2O5} (nm)	PBG in air (nm)	PBG in ethanol (nm)
(A)	174	(111): 328	(111): 455
(B)	234	(111): 451	(111): 610, (220): 375
(C)	277	(111): 510	(111): 675, (220): 410
(D)	304	(111): 565	(111): 750, (220): 462, (311): 395
(E)	324	(111): 595, (220): 365	(111): 775, (220): 475, (311): 400

Table 3
PBG positions and PBG ratios with respect to the (111) facets for Ta_2O_5 IO powders in ethanol.

Sample	PBG for Ta_2O_5 IO filled with ethanol (nm)	$\frac{\lambda_{(220)}}{\lambda_{(111)}}$	$\frac{\lambda_{(311)}}{\lambda_{(111)}}$
(A)	(111): 455	–	–
(B)	(111): 610 (220): 375	0.614	–
(C)	(111): 675 (220): 410	0.607	–
(D)	(111): 750 (220): 462 (311): 395	0.616	0.526
(E)	(111): 775 (220): 475 (311): 400	0.613	0.516

fluids filling the macropores. Fig. 7(c) reveals a linear relationship between the (111) and (220) PBGs and the refractive index of the medium filling the macropores, demonstrating that the polycrystalline Ta_2O_5 IO powders can be applied for the refractive index sensing of solvents.

Fig. 8(a) shows the diffuse reflectance spectra and digital images of the Ta_2O_5 (B) IO samples prepared by heating the PMMA (B)/Ta_2O_5 composites in air or nitrogen atmosphere. The (111) PBG position appeared at 450 nm in both the samples, resulting in a blue color. However, the removal of the PMMA template in a nitrogen atmosphere significantly enhanced the blue structural color of the sample. Under such conditions, a PMMA template will not fully burn out as carbon dioxide but instead leave a thin carbon residue that accentuates the structural color [15]. The same accentuation of the structural color by dark pigments is often observed in the natural world, such as in the iridescent feathers of many birds, where melanosomes either directly give rise to or enhance the structural color. Fig. 8(b) and (c) show the

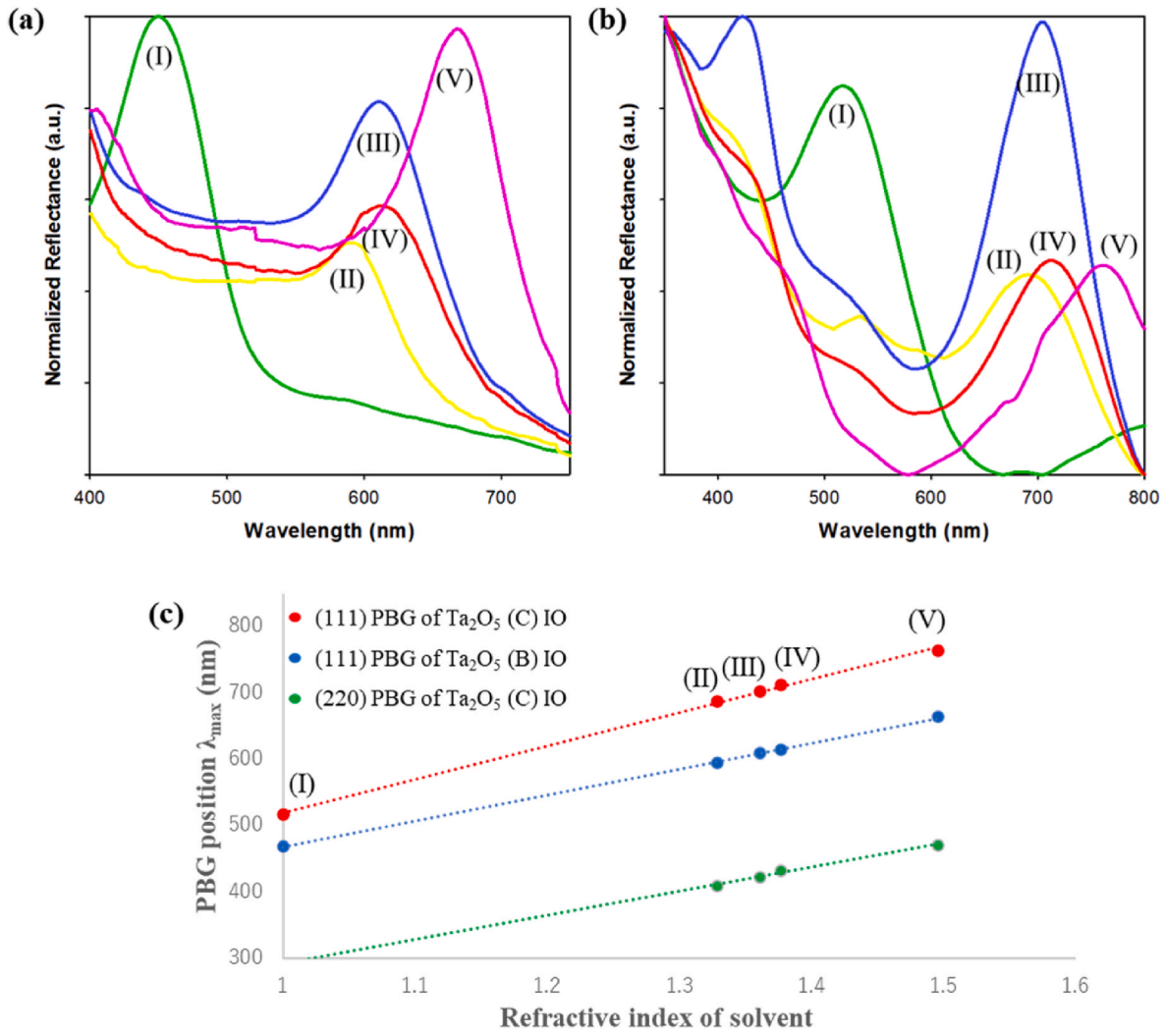

Fig. 7. UV–Vis diffuse reflectance spectra of Ta_2O_5 IO powders filled with air and solvents of different refractive indices (a) Ta_2O_5, (B) IO, and (b) Ta_2O_5, and (C) IO. Media in the macropores are (I) air, $n = 1.000$; (II) methanol, $n = 1.329$; (III) ethanol, $n = 1.360$; (IV) 2-propanol, $n = 1.377$; and (V) toluene, n = 1.496. (c) Plot of the PBG position versus the solvent refractive index.

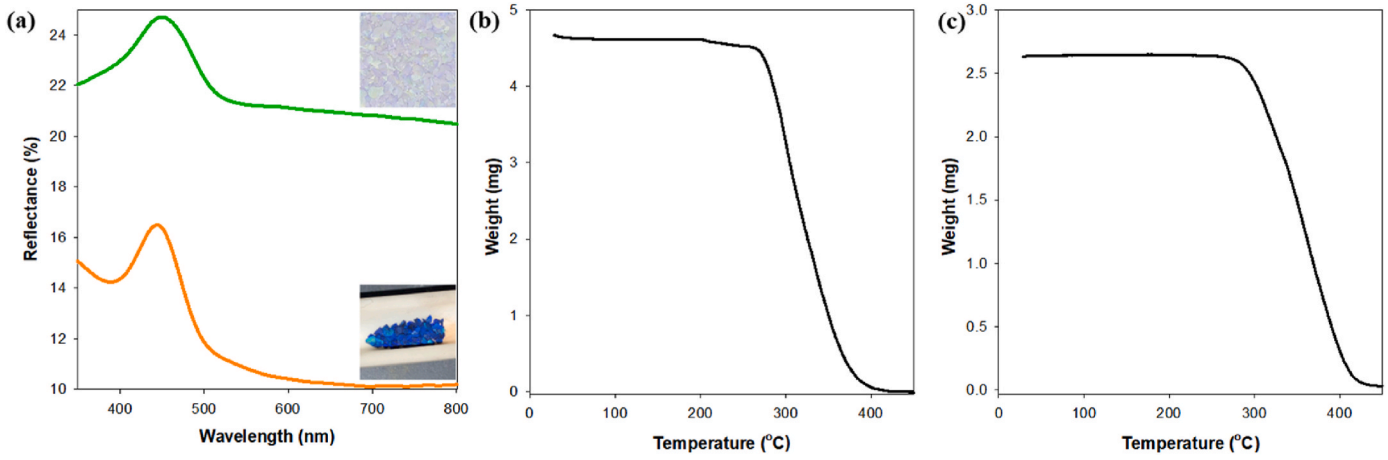

Fig. 8. (a) Diffuse reflectance spectra of Ta_2O_5 (B) IO prepared by heating in air (green line) or in a nitrogen atmosphere (orange line). TGA curves for PMMA colloids under heating in (b) air, or (c) N_2.

TGA curves of the PMMA colloids heated in air or a nitrogen atmosphere. When heated in air, all the PMMA was removed as carbon dioxide, leaving no residue behind. Upon heating under N_2, PMMA decomposed to form small hydrocarbons, leaving a carbon residue (~1 % of the initial mass of the PMMA). Hence, the Ta_2O_5 (B) IO prepared in N_2 atmosphere appeared darker with a more vivid structural color than

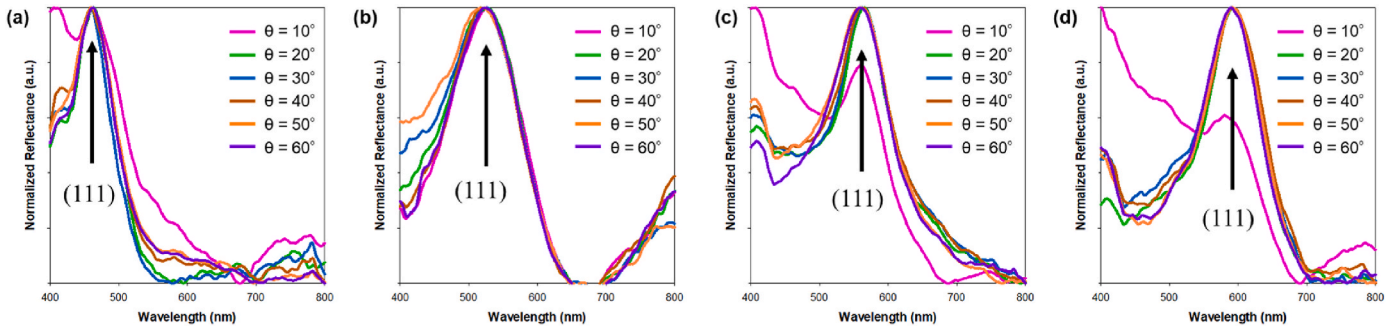

Fig. 9. Absolute reflectance spectra of Ta_2O_5 IO samples on changing the incidence angle from 10° to 60°: (a) Ta_2O_5 (B) IO; (b) Ta_2O_5 (C) IO; (c) Ta_2O_5 (D) IO; and (d) Ta_2O_5 (E) IO.

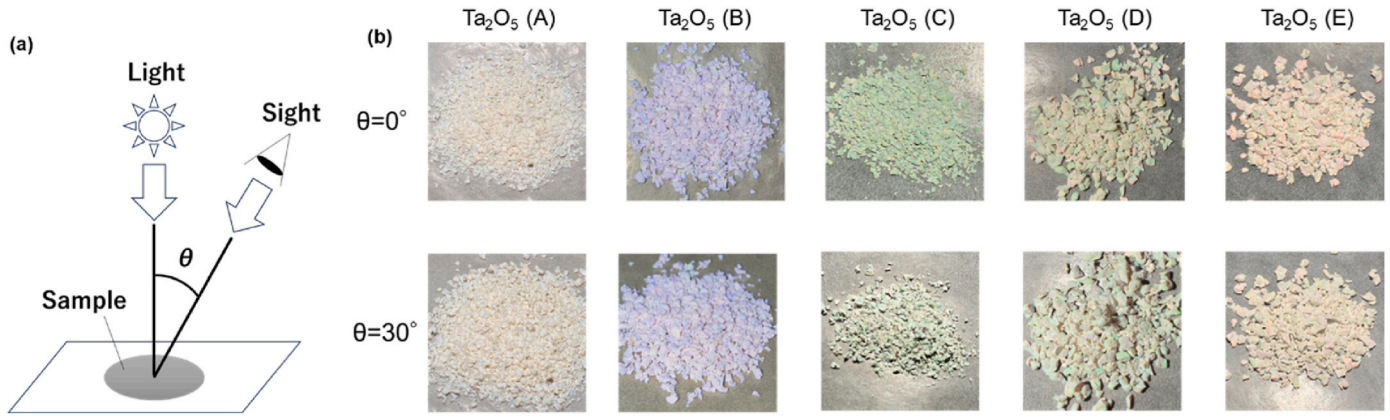

Fig. 10. Ta_2O_5 (A)–(E) IO powder colors at different incidence angles: (a) Schematic of the digital image capture geometry, (b) Digital images of different Ta_2O_5 IO samples in response to changes in the incidence angle.

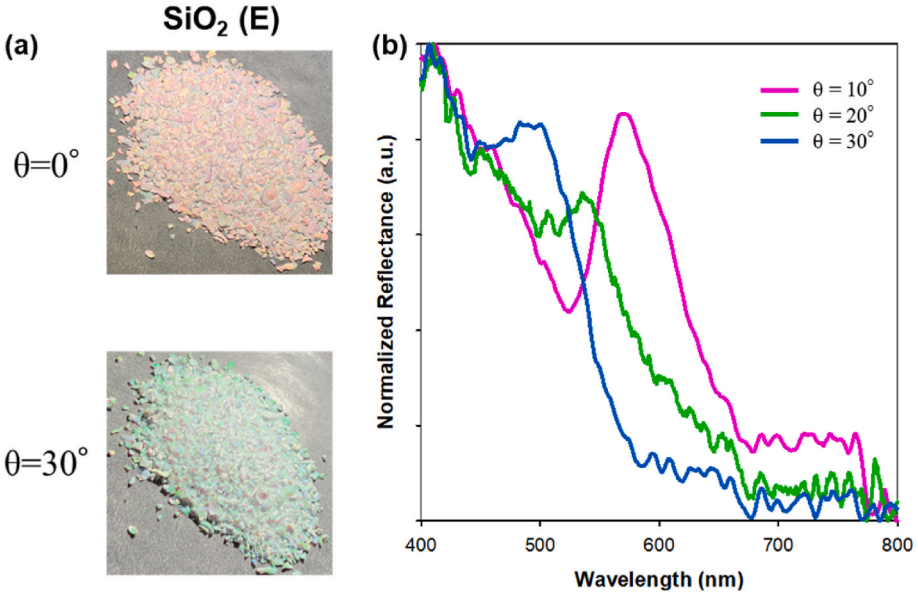

Fig. 11. Optical characterization of SiO_2 (E) IO powder: (a) Digital images of SiO_2 (E) IO at two different incidence angles, and (b) absolute reflectance spectra of SiO_2 (E) IO at different incidence angles.

the sample synthesized by calcination in air.

Angle-dependent color changes or iridescence are characteristic features of PhCs that are often used to distinguish PhC-generated color from pigment-based colors. Fig. 9 shows the absolute reflectance spectra of various Ta_2O_5 IO powders at different incidence angles. With the change in the incidence angle from 10° to 60°, the (111) PBG position in each sample remained largely unaffected. Fig. 10 shows the colors of the Ta_2O_5 IO samples at different incidence angles. As shown in Fig. 10(a), the incidence angle changed from 0 to 30°, and images of the powders were captured at both angles. Fig. 10(b) shows the digital images of the

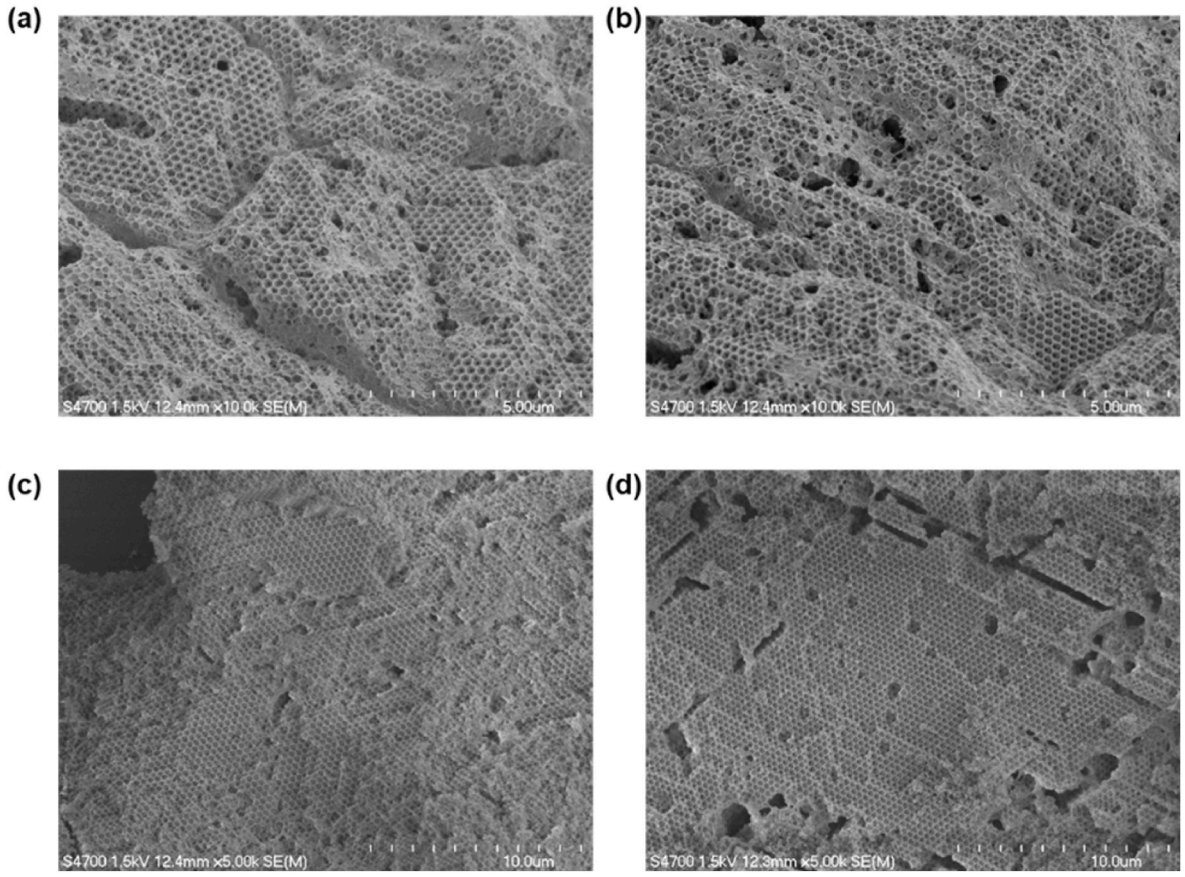

Fig. 12. SEM images (at different magnifications) of (a, b) Ta_2O_5 (E) IO, and (c, d) SiO_2 (E) IO.

Ta_2O_5 (A)–(E) IO powders, exhibiting their structural color. Consistent with the absolute reflection measurements, the color of the samples hardly changed with the incidence angle.

In contrast, the SiO_2 IO powder prepared using batch (E) PMMA colloids showed a distinct change in the color with the incidence angle (Fig. 11). The sample color showed a marked blue shift with increasing incident angle, while the (111) PBG moved to progressively shorter wavelengths as the incident angle increased from 10° to 30° (as predicted by Equation (3)).

The difference in the optical responses of the polycrystalline Ta_2O_5 IO and SiO_2 IO powders on changing the incidence angle can be explained as follows. Amorphous SiO_2 has a low refractive index (n = 1.45). As result PBGs in SiO_2 IOs tend to be quite narrow and well-separated at all incidence angles. Ta_2O_5 has a much higher refractive index of 2.1, which results in a significantly wider PBGs along the (111), (220), and (311) directions compared with silica-based IOs [7]. Generally, for a particular FCC plane, e.g. FCC (111) plane, the full-width-at-half-maximum of the PBG peak in reflectance spectra depends on a number of factors, including the solid volume fraction in the inverse opals (FWHM increases as the solid volume fraction decreases) as well as the refractive index of the materials in the walls of the inverse opals (FWHM increases as the refractive index of the solid material in

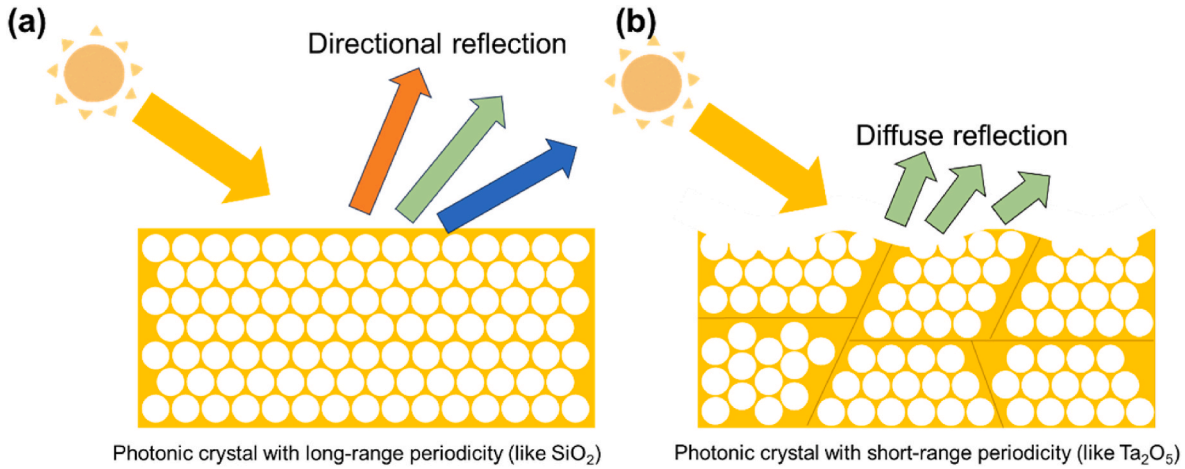

Fig. 13. Schematics of the inverse opal photonic crystals with (a) long-range order and angle-dependent color and (b) shorter-range order and minimal angle-dependent color.

the walls increases). In the case of Ta_2O_5 IOs, the large FWHM of each PBG peak increases the likelihood of an overlap of PBGs for different crystal planes with the change in the incidence angle (i.e., as the (111) PBG blueshifts with increasing angle with respect to the [111] direction, the PBGs on the other FCC planes like (220) and (311) may redshift as the incidence angle correspondingly decreases with respect to the surface normal of these planes, increasing the likelihood of overlapping PBGs). The overlapping of the PBGs on different planes at specific angles could mask the usual blueshift of the PBGs observed on particular planes with increasing incidence angle. A second factor that may have prevented an evident color change with the incidence angle in the Ta_2O_5 IO powders was the size of the exposed crystalline domains [1,38–41]. For the SiO_2 IO powder, the powder particles exhibited large domains with the same crystallographic orientation (Fig. 12), with much fewer defects than those observed in the Ta_2O_5 IO powders. Accordingly, stronger diffraction could occur on specific FCC planes, such as the dominant (111) planes, with the scattering caused by defects minimized. In the case of the Ta_2O_5 IO powders, the crystalline domains were much smaller, and the planes had more defects. Accordingly, the orientation of the various planes in the powdered samples was significantly more statistically random, along with more light scattering caused by defects, leading to more diffuse reflectance and broader PBGs which effectively eliminated the typically-seen angular PBG dependence (Fig. 13). In short, at all incidence angles, the types and abundance of planes exposed by the Ta_2O_5 IOs were the same. Hence, no change in the color was observed with the viewing angle (i.e., angle effects were averaged out).

This study demonstrated that the angle dependence of the PBG position in polycrystalline IO powders can be very different from that observed in thin films with specific orientations (i.e., (111) planes parallel to the underlying substrate, as is typically studied in the PhC field). The short-range periodicities of Ta_2O_5 IOPhCs are not ideal from an optical-quality perspective. Nevertheless, many applications require materials that do not change color over a wide range of viewing angles, such as pigment applications and photocatalysis [42–45].

4. Conclusions

Polycrystalline Ta_2O_5 IO powders with varying macropore diameters and PBGs at UV and visible wavelengths were successfully fabricated using the colloidal crystal templating method. Filling the interstitial voids in PMMA colloidal crystal templates using a vacuum-assisted immersion impregnation method was found to be beneficial for producing brightly colored Ta_2O_5 IOPhCs. The PBGs in the Ta_2O_5 IO powders redshifted with the macropore diameter in the IOs and also with increasing refractive index of the medium filling the macropores, in accordance with the modified Bragg's equation. Similar to other IO materials containing a highly dielectric material in the walls (such as TiO_2) and surface defects, the polycrystalline Ta_2O_5 IO powders did not show a significant change in color with the viewing angle under white-light irradiation.

Submission declaration and verification

The authors declare that this work has not been published previously (except in the form of an abstract, a published lecture or academic thesis), that it is not under consideration for publication elsewhere, and that its publication is approved by all authors and tacitly or explicitly by the responsible authorities where the work was carried out.

CRediT authorship contribution statement

Taiki Maekawa: Writing – original draft, Visualization, Methodology, Investigation, Conceptualization. **Hiroyuki Maekawa:** Validation, Investigation. **Yuto Ikeda:** Investigation. **Tomoya Onoe:** Investigation. **Geoffrey I.N. Waterhouse:** Writing – review & editing, Methodology, Conceptualization. **Kei-ichiro Murai:** Validation, Supervision, Resources. **Toshihiro Moriga:** Writing – review & editing, Supervision, Resources, Project administration, Funding acquisition.

Declaration of competing interest

The authors declare that they have no known competing financial interests or personal relationships that could have appeared to influence the work reported in this paper.

Acknowledgments

This work was supported by JST SPRING, Grant Number JPMJSP2113, and by JSPS KAKENHI Grant Numbers JP18H02059 and JP24K08567.

References

[1] Taiki Maekawa, et al., Slow photon photocatalytic enhancement of H_2 production in TaON inverse opal photonic crystals, J. Solid State Chem. 329 (2024) 124404, https://doi.org/10.1016/j.jssc.2023.124404.
[2] Yongfa Zhu, et al., Preparation and performances of nanosized Ta_2O_5 powder photocatalyst, J. Solid State Chem. 178 (1) (2005) 224–229, https://doi.org/10.1016/j.jssc.2004.11.015.
[3] Yoshiko Takahara, et al., Synthesis and application for overall water splitting of transition metal-mixed mesoporous Ta oxide, Solid State Ionics 151 (1–4) (2002) 305–311, https://doi.org/10.1016/S0167-2738(02)00728-2.
[4] Kazuhiko Maeda, et al., Surface modification of TaON with monoclinic ZrO_2 to produce a composite photocatalyst with enhanced hydrogen evolution activity under visible light, Bull. Chem. Soc. Jpn. 81 (8) (2008) 927–937, https://doi.org/10.1246/bcsj.81.927.
[5] Daisuke Nakauchi, et al., Photoluminescence and scintillation properties of Tb: $GdTaO_4$ crystals, Sensor. Mater. 33 (2021) 2203, https://doi.org/10.18494/SAM.2021.3323.
[6] Eli Yablonovitch, Inhibited spontaneous emission in solid-state physics and electronics, Phys. Rev. Lett. 58 (20) (1987) 2059, https://doi.org/10.1103/PhysRevLett.58.2059.
[7] E.J.J.B. Yablonovitch, Photonic band-gap structures, JOSA B. 10 (2) (1993) 283–295, https://doi.org/10.1364/JOSAB.10.000283.
[8] Pierre R. Villeneuve, Piche Michel, Photonic bandgaps in periodic dielectric structures, Prog. Quant. Electron. 18.2 (1994) 153–200, https://doi.org/10.1016/0079-6727(94)90007-8.
[9] Mariano Curti, et al., Inverse opal photonic crystals as a strategy to improve photocatalysis: underexplored questions, J. Phys. Chem. Lett. 6 (19) (2015) 3903–3910, https://doi.org/10.1021/acs.jpclett.5b01353.
[10] Jing Liu, et al., Slow photons for photocatalysis and photovoltaics, Adv. Mater. 29 (17) (2017) 1605349, https://doi.org/10.1002/adma.201605349.
[11] Ping Li, et al., Probing photon localization effect between titania and photonic crystals on enhanced photocatalytic activity of titania film, Chem. Eng. J. 284 (2016) 305–314, https://doi.org/10.1016/j.cej.2015.08.094.
[12] Olivier Deparis, S.R. Mouchet, B.-L. Su, Light harvesting in photonic crystals revisited: why do slow photons at the blue edge enhance absorption? Phys. Chem. Chem. Phys. 17 (45) (2015) 30525–30532, https://doi.org/10.1039/C5CP04983K.
[13] Sajeev John, Strong localization of photons in certain disordered dielectric superlattices, Phys. Rev. Lett. 58 (23) (1987) 2486, https://doi.org/10.1103/PhysRevLett.58.2486.
[14] Eileen Armstrong, Colm O'Dwyer, Artificial opal photonic crystals and inverse opal structures–fundamentals and applications from optics to energy storage, J. Mater. Chem. C 3 (24) (2015) 6109–6143, https://doi.org/10.1039/C5TC01083G.
[15] David P. Josephson, Matthew Miller, Andreas Stein, Inverse opal SiO_2 photonic crystals as structurally-colored pigments with additive primary colors, Z. Anorg. Allg. Chem. 640 (3) (2014) 655–662, https://doi.org/10.1002/zaac.201300578, 4.
[16] E.A. Gaulding, et al., Fabrication and optical characterization of polystyrene opal templates for the synthesis of scalable, nanoporous (photo) electrocatalytic materials by electrodeposition, J. Mater. Chem. A 5 (23) (2017) 11601–11614, https://doi.org/10.1039/C7TA00512A.
[17] Zuocheng Zhou, X.S. Zhao, Opal and inverse opal fabricated with a flow-controlled vertical deposition method, Langmuir 21 (10) (2005) 4717–4723, https://doi.org/10.1021/la046775t.
[18] Jie Yu, et al., TiO_2 inverse opal photonic crystals: synthesis, modification, and applications-A review, J. Alloys Compd. 769 (2018) 740–757, https://doi.org/10.1016/j.jallcom.2018.07.357.
[19] Jian Qin, et al., Synthesis of three-dimensionally ordered macroporous $LaFeO_3$ with enhanced methanol gas sensing properties, Sensor. Actuator. B Chem. 209 (2015) 706–713, https://doi.org/10.1016/j.snb.2014.12.046.
[20] Jing Liu, et al., Slow photon-enhanced heterojunction accelerates photocatalytic hydrogen evolution reaction to unprecedented rates, CCS Chem. 5 (2) (2023) 372–384, https://doi.org/10.31635/ccschem.022.202101699.
[21] Xiaofeng Cui, et al., A photonic crystal-based CdS–Au–WO_3 heterostructure for efficient visible-light photocatalytic hydrogen and oxygen evolution, RSC Adv. 4 (30) (2014) 15689–15694, https://doi.org/10.1039/C4RA01415D.

[22] Xuesong Qu, et al., Preparation and photoluminescence properties of Gd_2O_3:Eu^{3+} inverse opal photonic crystals, J. Phys. Chem. C 114 (47) (2010) 19891–19894, https://doi.org/10.1021/jp104621y.
[23] Zhengwen Yang, et al., Energy transfer enhancement in Eu^{3+} doped $TbPO_4$ inverse opal photonic crystals, J. Appl. Phys. 105 (8) (2009) 083523, https://doi.org/10.1063/1.3112007.
[24] Geoffrey IN. Waterhouse, et al., Achieving color and function with structure: optical and catalytic support properties of ZrO_2 inverse opal thin films, ACS Omega 3 (8) (2018) 9658–9674, https://doi.org/10.1021/acsomega.8b01334.
[25] Geoffrey IN. Waterhouse, et al., Structural, optical, and catalytic support properties of γ-Al_2O_3 inverse opals, J. Phys. Chem. C 119 (12) (2015) 6647–6659, https://doi.org/10.1021/acs.jpcc.5b00437.
[26] Geoffrey IN. Waterhouse, et al., Physical and optical properties of inverse opal CeO_2 photonic crystals, Chem. Mater. 20 (3) (2008) 1183–1190, https://doi.org/10.1021/cm703005g.
[27] Geoffrey IN. Waterhouse, Mark R. Waterland, Opal and inverse opal photonic crystals: fabrication and characterization, Polyhedron 26 (2) (2007) 356–368, https://doi.org/10.1016/j.poly.2006.06.024.
[28] Yusong Dong, et al., Optical and photocatalytic properties of three-dimensionally ordered macroporous Ta_2O_5 and Ta_3N_5 inverse opals, Chem. Mater. (2023), https://doi.org/10.1021/acs.chemmater.3c01903.
[29] Masahiro Sadakane, et al., Three-dimensionally ordered macroporous (3DOM) materials of spinel-type mixed iron oxides. Synthesis, structural characterization, and formation mechanism of inverse opals with a skeleton structure, Bull. Chem. Soc. Jpn. 80 (4) (2007) 677–685, https://doi.org/10.1246/bcsj.80.677.
[30] Masahiro Sadakane, et al., Preparation of three-dimensionally ordered macroporous perovskite-type lanthanum–iron-oxide $LaFeO_3$ with tunable pore diameters: high porosity and photonic property, J. Solid State Chem. 183 (6) (2010) 1365–1371, https://doi.org/10.1016/j.jssc.2010.04.012.
[31] Xuyang Zhang, et al., Synthesis of metal oxide inverse opals from metal nitrates by PMMA colloidal crystal templating, Eur. J. Inorg. Chem. 35 (2020) 3402–3407, https://doi.org/10.1002/ejic.202000517, 2020.
[32] Rick C. Schroden, et al., Optical properties of inverse opal photonic crystals, Chem. Mater. 14 (8) (2002) 3305–3315, https://doi.org/10.1021/cm020100z.
[33] Andreas Stein, Li Fan, Nicholas R. Denny, Morphological control in colloidal crystal templating of inverse opals, hierarchical structures, and shaped particles, Chem. Mater. 20 (3) (2008) 649–666, https://doi.org/10.1021/cm702107n.
[34] Heng Zhao, et al., Blue-edge slow photons promoting visible-light hydrogen production on gradient ternary 3DOM TiO_2-Au-CdS photonic crystals, Nano Energy 47 (2018) 266–274, https://doi.org/10.1016/j.nanoen.2018.02.052.
[35] Peter G. Bolhuis, et al., Entropy difference between crystal phases, Nature 388 (6639) (1997) 235–236, https://doi.org/10.1038/40779.
[36] L.V. Woodcock, Entropy difference between the face-centred cubic and hexagonal close-packed crystal structures, Nature 385 (6612) (1997) 141–143, https://doi.org/10.1038/385141a0.
[37] Carlos I. Aguirre, Edilso Reguera, Andreas Stein, Tunable colors in opals and inverse opal photonic crystals, Adv. Funct. Mater. 20 (16) (2010) 2565–2578, https://doi.org/10.1002/adfm.201000143.
[38] Harun Ur, Mohammad Rashid, et al., Angle-independent structural color in colloidal amorphous arrays, ChemPhysChem 11 (3) (2010) 579–583, https://doi.org/10.1002/cphc.200900869.
[39] Jong Bin Kim, et al., Designing structural-color patterns composed of colloidal arrays, ACS Appl. Mater. Interfaces 11 (16) (2019) 14485–14509, https://doi.org/10.1021/acsami.8b21276.
[40] Carlos I. Aguirre, Edilso Reguera, Andreas Stein, Colloidal photonic crystal pigments with low angle dependence, ACS Appl. Mater. Interfaces 2 (11) (2010) 3257–3262, https://doi.org/10.1021/am100704f.
[41] Lei Shi, et al., Amorphous photonic crystals with only short-range order, Adv. Mater. 25 (37) (2013) 5314–5320, https://doi.org/10.1002/adma.201301909.
[42] Dongpeng Yang, et al., Facile synthesis of monodispersed SiO_2@Fe_3O_4 core–shell colloids for printing and three-dimensional coating with noniridescent structural colors, ACS Omega 4 (1) (2019) 528–534, https://doi.org/10.1021/acsomega.8b02987.
[43] Ning Sun, et al., Enhancing the brightness and saturation of noniridescent structural colors by optimizing the grain size, Nanoscale Adv. 2 (10) (2020) 4581–4590, https://doi.org/10.1039/D0NA00609B.
[44] Jin-Gyu Park, et al., Full-Spectrum photonic pigments with non-iridescent structural colors through colloidal assembly, Angew. Chem. Int. Ed. 53 (11) (2014) 2899–2903, https://doi.org/10.1002/anie.201309306.
[45] Jue Hou, Mingzhu Li, Yanlin Song, Patterned colloidal photonic crystals, Angew. Chem. Int. Ed. 57 (10) (2018) 2544–2553, https://doi.org/10.1002/anie.201704752.